INORGANIC CHEMISTRY FRONTIERS

RESEARCH ARTICLE

View Article Online
View Journal

Cite this: DOI: 10.1039/d2qi00187j

Symmetry-breaking phase transitions, dielectric and magnetic properties of pyrrolidinium-tetrahalidocobaltates†

Martyna Książdzyna,[a] Vasyl Kinzhybalo,[b] Alina Bieńko,[a] Wojciech Medycki,[c] Ryszard Jakubas,[a] Cyril Rajnák,[d] Roman Boča,[d] Andrew Ozarowski,[e] Mykhaylo Ozerov[e] and Anna Piecha-Bisiorek*[a]

We report the physicochemical characteristics of novel Co-based pyrrolidinium analogs: $(C_4H_{10}N)_2CoCl_4$ (**PCC**) and $(C_4H_{10}N)_2CoBr_4$ (**PCB**). Both compounds consist of a zero-dimensional (0D) anionic network and disordered pyrrolidinium cations. The structural origin of the anomalies observed in the electrical measurements has been confirmed by DSC thermograms and X-ray analysis. The crystals under investigations undergo a complex sequence of phase transitions: **PCC** at 347/353 K (phase **I** ↔ phase **II**) and 202/257 K (**II** ↔ **III**) and **PCB** at 380/381 K (**I** ↔ **II**) and 256/302 K (**II** ↔ **III**). The molecular motions of cations in both compounds were analysed based on proton magnetic resonance (^{1}H NMR and M_2) measurements, while their magnetic properties were investigated in DC and AC modes. The DC data show magnetic anisotropy, which was confirmed by high-field HF EPR measurements. The AC susceptibility data of **PCC** reveal slow magnetic relaxation at the applied DC field with two relaxation channels. Given the above this organic–inorganic hybrid can be considered as a rare example of multifunctional materials which exhibit dielectric and magnetic activity.

Received 24th January 2022,
Accepted 26th March 2022

DOI: 10.1039/d2qi00187j

rsc.li/frontiers-inorganic

1. Introduction

Organic–inorganic hybrid materials based on metallohalides (M = Co(II), Fe(II) Zn(II), Mn(II) Cu(II) *etc.*) form a large family of compounds exhibiting structural phase transition (PT). Diverse structures were found for these compounds, varying from zero-dimensional (0D) clusters, one-dimensional (1D) chains, two-dimensional (2D) layers to 3D frameworks. The structural diversity is caused mainly by the versatile metal–halide bonds and differing size and symmetry of the organic cations. Increased interest has been observed recently in metallohalide materials showing structural PTs, especially those exhibiting distinct dielectric anomalies. The crystal structures of 0D halidometallates(II) contain discrete $[MX_4]^{2-}$ components. Despite their apparent structural simplicity, alkyl-ammonium and phosphonium/arsonium tetrahalidometallates of d-block and other metals ($[NR_4]_n^+[MX_4]^{n-}$, where R = Me, Et, *etc.*, X = Cl, Br and n = 1 or 2) exhibit a rich diversity of ferromagnetic, ferroelectric, ferroelastic and incommensurate phases (Sawada *et al.*,[1] Shimizu *et al.*,[2] Styczeń *et al.*,[3,4] Zubillaga *et al.*,[5] Clay *et al.*,[6] and Pressprich *et al.*[7]). Tetramethylammonium analogs deserve special attention because these materials have become canonical models for studying disordered incommensurate–commensurate phase sequences (Lopez-Echarri *et al.*).[8] It has turned out that for all materials in this class, the relationships between phases are conditioned by the orientations of component ions which undergo subtle changes with temperature (Barreda-Argüeso *et al.*).[9]

In the case of halidocobaltate(II) hybrids, literature reports on organic–inorganic compounds exhibiting switchable dielectric properties are quite rare, except for tetraalkyl-ammonium and -phosphonium analogues. Most examples concern tetrahalidocobaltates(II) characterized by 0D structures with various polar cations *e.g.*; 3-chloro-2-hydroxypropyl trimethylammonium,[10] (H_2dabco-C_2H_5),[11] 1,4-diisopropyl-1,4-diazonia-bicyclo-[2.2.2] octane,[12] trimethylchloromethyl ammonium,[13] (*N*,*N*-dimethylbenzylammonium),[14] triethylbenzylammonium,[15] methyl-

[a]Faculty of Chemistry, University of Wrocław, F. Joliot-Curie 14, 50-383 Wrocław, Poland. E-mail: anna.piecha@chem.uni.wroc.pl
[b]Institute of Low Temperature and Structure Research Polish Academy of Sciences, Okólna 2, 50-422 Wrocław, Poland
[c]Institute of Molecular Physics, Polish Academy of Sciences, M. Smoluchowskiego 17, 60-179 Poznań, Poland
[d]Department of Chemistry, Faculty of Natural Sciences, University of SS Cyril and Methodius, 91701 Trnava, Slovakia
[e]National High Magnetic Field Laboratory, Florida State University, 1800 East Paul Dirac Drive, Tallahassee, Florida 32310, USA

† Electronic supplementary information (ESI) available. CCDC 2082868–2082871. For ESI and crystallographic data in CIF or other electronic format see DOI: https://doi.org/10.1039/d2qi00187j

triphenylphosphonium,[16] $[NH_2(C_2H_5)_2]$,[17] $[(CH_2)_7(NH_3)_2]$,[18] ethylammonium,[19] and methylammonium.[20] Structural instability in these compounds is due to the dynamics of the organic cations. Ferroelectric properties within this type of compound are unique. To the best of our knowledge, only three ferroelectrics have been synthesized so far; the dimethylammonium analog – $[NH_2(CH_3)_2]_2CoCl_4$,[21] PT ($P2_1/n \rightarrow$ polar) and *n*-dodecylammonium – $(C_{12}H_{25}NH_3)_2CoCl_4$.[22] The most interesting appears to be an organic–inorganic hybrid (diisobutylammonium)$_3$ClCoCl$_4$, with a high Curie temperature of 372.5 K and significant spontaneous polarization of 4.6 μC cm^{-2}. This is the first example of a hybrid photosensitive ferroelectric that is strongly sensitive to specific wave band illumination.[23]

Recently, we have synthesized and characterized a novel cobaltate(II) organic–inorganic hybrid based on the imidazolium cation – $(C_3N_2H_5)_2CoCl_4$ (**ICC**).[24] This compound was found to undergo two structural PTs: a continuous one at 245.5 K (from phase I to II) and a discontinuous one at 234/237 K (cooling/heating) (II → III). **ICC** crystallizes in the monoclinic space groups *C*2/*c* and $P2_1/c$ in phase (I) and (III), respectively. The intermediate phase (II) appeared to be incommensurately modulated. The dielectric spectroscopy and proton magnetic resonance (^{1}H NMR) studies showed that the dynamics of imidazolium cations contributes mainly to the PT mechanism in **ICC**. Additionally, this analog revealed weak antiferromagnetic properties. In recent literature reports, pyrrolidine appears more and more often as a cation with a permanent dipole moment in organic–inorganic hybrids, which is associated with large possibilities of reorientation of the cation in the crystal lattice.[24–29] This probably increases the chance of phase changes and, consequently, promising physicochemical properties. Among the compounds, one can distinguish a group containing metals M^{2+}: for example pyrrolidinium trichloridocuprate $(C_4NH_{10})CuCl_3$, which crystallizes in α and β forms in the *C*2/*c* space group.[30,31] Studies with a more broad spectrum were carried out for pyrrolidinium derivatives based on Mn(II): $(C_4NH_{10})MnCl_3$ and $(C_4NH_{10})MnBr_3$, which additionally exhibit luminescence properties.[32,33] Moreover, it should be noted that both compounds are ferroelectrics, and the bromide derivative also exhibits ferromagnetic properties. Recently, we have synthesized and characterized two pyrrolidinium analogs based on Sb(III); $(C_4NH_{10})_3[Sb_2Cl_9]$[25] and $(C_4NH_{10})_2[SbCl_5]$.[34] In all pyrrolidinium halogenometallate hybrids dynamics of cations plays a key role in the mechanism of PTs.

Halidocobaltate(II) hybrids can be also obvious leaders in the field of magnetic materials due to their ability to construct SIM materials that exhibit slow magnetization relaxation, which may have potential applications in high-density information storage, spintronics and quantum processing. Experimental and theoretical calculations suggest that a high-spin Co(II) ion, which may exhibit large magnetic anisotropy with a flexible zero field splitting parameter with both an easy-axis ($D < 0$) and an easy-plane anisotropy ($D > 0$) depending on its coordination geometry and the distortion degree of its surroundings, is an excellent candidate for building SIMs.[35,36] In this respect, examples of SIMs with this metal ion include trigonal planar,[37] tetrahedral,[38,39] square-pyramidal,[40,41] trigonal bipyramidal,[42] octahedral,[43] pentagonal bipyramidal,[44] and square antiprism[45] mononuclear complexes as well as a few coordination polymers containing six-coordinate cobalt(II) ions.[46]

Special attention, for example, has been paid to establishing a magneto-structural correlation based on *D* for low-coordinated tetrahedral Co(II) mononuclear compounds, for which the magnetic anisotropy can be considerably influenced not only by the variations in the first and second coordination spheres but also by the type of terminal ligand and the nature of metal–ligand covalent bonding.[47–49] In particular, it has been shown that heavier and softer terminal ligands are able to modify significantly the anisotropy of Co(II) centers.[50,51] The breakthrough work of this area was the example of a homoleptic mononuclear compound $[PPh_4]_2[Co(SPh)_4]$ reported by Zadrozny *et al.*, which possesses a large negative ZFS parameter *D*, −70 cm^{-1}, and exhibits SIM behaviour in a zero static magnetic field.[50] So, a combination of the functional properties of both ingredients (organic and inorganic) makes this field of research very attractive.

In search for new non-centrosymmetric cobaltate(II) organic–inorganic hybrids we have embedded in the crystal structure unsymmetrical pyrrolidinium cations. Herein, in the process of designing new switchable dielectric PT materials, we synthesized two 0D organic–inorganic hybrid compounds based on Co(II): $(C_4H_{10}N)_2CoCl_4$ (**PCC**) and $(C_4H_{10}N)_2CoBr_4$ (**PCB**), which exhibit a complex sequence of PTs. Moreover, cation dynamics gives rise to interesting dielectric properties. The molecular motions of pyrrolidinium cations have been studied by means of relaxation measurements in proton magnetic resonance (^{1}H NMR). The magnetic properties of mononuclear Co(II) complexes were also studied. The results obtained in this work suggest new pathways for further research on ferroic materials based on cobalt–chloride/bromide hybrid organic–inorganic derivatives.

2. Experimental

2.1 Synthesis

All reagents in the synthesis were of reagent grade purity and were used as commercially obtained.

$(C_4H_{10}N)_2CoBr_4$ (**PCB**) crystals were prepared by the reaction of cobalt(II) bromide ($CoBr_2$, Sigma-Aldrich 99%) dissolved in distilled water and pyrrolidine (C_4H_8NH, Sigma-Aldrich >99.5%) at molar ratio 1 : 1 in concentrated hydrobromic acid (HBr, Sigma-Aldrich 48%). The mixture was left to stand for several days and needle-shaped blue crystals were obtained.

$(C_4H_{10}N)_2CoCl_4$ (**PCC**) blue needle like crystals were obtained in a similar way ($CoCl_2$, Sigma-Aldrich 99%) and concentrated 36% HCl was used. Both materials are highly hygroscopic.

The results of the elemental analysis for C/N/H are close to theoretical ones (Table S1†), and the experimental PXRD is well consistent with the corresponding simulated one indicating the phase purity of the two title compounds (Fig. S1†).

2.2 Thermal analysis

Differential Scanning Calorimetry (DSC) experiments were performed on a PerkinElmer model 8500 differential scanning calorimeter calibrated using *n*-heptane and indium, under a nitrogen atmosphere in hermetically sealed Al pans on the polycrystalline material.

Simultaneous Thermogravimetric Analysis (TGA) and Differential Thermal Analysis (DTA) were performed on a Setaram SETSYS 16/18 instrument in the temperature range 300–900 K with a ramp rate of 2 K min^{-1} (Fig. S2†). The scans were performed in flowing nitrogen (flow rate: 1 dm^3 h^{-1}).

2.3 X-ray analysis

Diffraction data for **PCB** and **PCC** crystals were recorded on an Oxford Diffraction Xcalibur four-circle diffractometer with Mo Kα radiation (λ = 0.71073 Å) equipped with an Atlas CCD detector (section 3 in the ESI†). The collected diffraction data for all compounds were processed with the CrysAlis PRO program.[52] The structures were solved by direct methods using SHELXS or SHELXT programs and refined by the least squares method on F^2 by SHELXL software with the following graphical user interfaces of OLEX.[53,54] Atomic displacements for non-hydrogen atoms were refined using an anisotropic model. All hydrogen atoms were placed in ideal positions and refined as riding atoms with relative isotropic displacement parameters. The crystal parameters, data collection and the refinement are summarized in Table S2.† The crystallographic data for the material can also be obtained from the CCDC (no.: 2082868–2082871†).

2.4 Dielectric measurements

The complex dielectric permittivity, $\varepsilon^* = \varepsilon' - i\varepsilon''$, was measured with an Agilent E4980A Precision LCR Meter between 100 and 400 K in the frequency range between 135 Hz and 2 MHz. The overall error was less than 5%. The dielectric permittivities of the polycrystalline sample of **PCC** with about 16 mm^2 area and 1.2 mm thickness and the single crystal sample of **PCB** with about 6 mm^2 area and 0.7 mm thickness were measured. Conductive silver paste was stuck on the opposite faces of materials and used as electrodes.

2.5 Optical measurements

The ferroelastic domain structures of the **PCC** and **PCB** crystals were observed by means of an Olympus BX53 optical polarization microscope combined with a LINKAM THM-600 heating/cooling stage. The temperature was stabilized to within 0.1 K (more in section 4 (ESI†)).

2.6 Nuclear magnetic resonance

T_1 measurements were carried out as a function of temperature at 25 MHz using an ELLAB TEL-Atomic PS 15 spectrometer. The inversion recovery pulse sequence was used. The temperature of the sample was varied from 83 to 420 K using a UNIPAN 660 temperature controller operating on a Pt 100 sensor providing long time temperature stability better than 1 K. Single exponential magnetization decays were observed in the whole temperature range. The estimated average error of the measured T_1 values is 5%.

The second moment (M_2) data of the ^{1}H NMR line was measured on an ELLAB CW continuous wave spectrometer at the resonance frequency of 26.8 MHz. The second moment values were calculated by numerical integration of the first derivative of an absorption line and corrected for the finite modulation amplitude (more in section 5 (ESI†)).

2.7 EPR and far-infrared magnetic spectroscopy (FIRMS) studies

The high-field, high-frequency EPR spectra at temperatures ranging from *ca*. 3 K to 290 K were recorded on a home-built spectrometer at the EMR facility of the National High Magnetic Field Laboratory (NHMFL). The instrument is equipped with a superconducting magnet (Oxford Instruments) capable of reaching a field of 17 T. Microwave frequencies over the range 52–630 GHz were generated using a phase-locked Virginia Diodes source, producing a base frequency of 8–18 GHz, which was multiplied by a cascade of frequency multipliers. The instrument is a transmission-type device and uses no resonance cavity. Far Infrared Magnetic Spectroscopy was performed at the NHMFL on a 17 T vertical-bore superconducting magnet using a Bruker Vertex 80v Fourier-transform infrared spectrometer. The evacuated (~4 mBar) optical beamline was used for their coupling and the experimental set-up was equipped with a mercury lamp and a composite silicon bolometer (Infrared Laboratories), as a THz radiation source and detector, respectively. Eicosane pellets containing the studied compound were measured in the spectral region between 18 and 730 cm^{-1} (0.55–22 THz) with the resolution of 0.3 cm^{-1} (9 GHz). Both the sample and bolometer were cooled using low-pressure helium gas to the temperature of 4.6 K. Transmittance spectra were calculated as the THz intensity spectrum at each magnetic field divided by the THz intensity spectrum averaged for all fields.

2.8 Magnetic data

The DC magnetic data were recorded using a SQUID magnetometer (MPMS, Quantum Design) with *ca*. 22 mg of sample. The susceptibility data were acquired at B_{DC} = 0.5 T between T = 1.8 and 300 K. This was corrected for the underlying diamagnetism and transformed to the effective magnetic moment. The magnetization data were recorded at low temperatures T = 2.0 up to B_{max} = 5.0 T. No remnant magnetization has been detected. The AC susceptibility data were obtained with the same apparatus and the same samples using the amplitude of the oscillating field B_{AC} = 0.3 mT. Three regimes were used: (i) scan of the AC susceptibility as a function of the field up to B_{DC} = 1 T at T = 2.0 K for a set of four trial frequencies f; (ii) scan of the AC susceptibility as a function of temperature for 22 frequencies of the oscillating field and a set of temperatures ranging between T = 1.8 and 7.0 (8.0) K, all performed at the appropriately selected field B_{DC} = 0.2 (0.15) T.

3. Results

3.1 Thermal properties

DSC measurements (Fig. 1) show the occurrence of one transformation above and one below room temperature (RT). The transition between **I** and **II** is characterized by a small temperature hysteresis (1 K and 6 K, for **PCB** and **PCC** respectively), while the transition between **II** and **III** reveals a very large difference between the heating and cooling cycles: 46 K for **PCB** and 55 K for **PCC**.

The transition entropy for the PTs in **PCB** is significant: $\Delta S_{(I\rightarrow II)} = 7$ J K^{-1} mol^{-1} (380 K) and $\Delta S_{(II\rightarrow III)} = 10.0$ J K^{-1} mol^{-1} (256 K). Both PTs are evidently first order and the ΔS_{Tr} value proves the 'order–disorder' mechanism of these transitions. A quite similar phase situation occurs in the **PCC** compound. The corresponding transition entropy values are: $\Delta S_{(I\rightarrow II)} = 12$ J K^{-1} mol^{-1} (347 K) and $\Delta S_{(II\rightarrow III)} = 6.5$ J K^{-1} mol^{-1}. It should be noticed that total entropy changes for these two transitions for **PCB** and **PCC** are comparable (17 and 18.5 J K^{-1} mol^{-1}, respectively). The thermal stability of the compounds determined by TGA/DTA measurement is 400 K for **PCC** and 515 K for **PCB** (Fig. S2†).

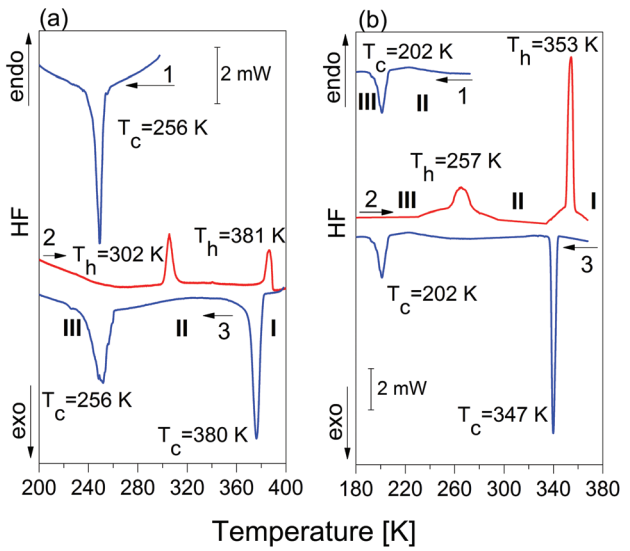

Fig. 1 DSC curves for (a) **PCB** (m = 13.250 mg) and (b) **PCC** (m = 12.985 mg) during cooling and heating samples.

3.2 Crystal structures of PCC and PCB

The room temperature phases of the title compounds, **PCC** and **PCB**, are not isomorphous (more in the ESI (part 3†)). The chloride analogue crystallizes in the monoclinic $P2_1/c$ space group type with the monoclinic angle being very close to 90° (within the experimental error). The measured crystal in this case demonstrated typical twinning with the following twin matrix {−1 0 0 0 −1 0 0 0 1}. The independent part of the structure consists of four $[CoCl_4]^{2-}$ anions and eight $(C_4H_{10}N)^+$ cations (Z' = 4) (Fig. 2(a)). The bromide analog crystallizes in the monoclinic $P2_1/n$ space group with only one $[CoBr_4]^{2-}$ anion and two $(C_4H_{10}N)^+$ cations (Z' = 1) in the independent part of the structure (Fig. 2(b)). The monoclinic angle deviates by ~3.7° from a right angle.

One may notice the similarities in the crystal packing projections of room temperature phases of chloride and bromide analogues (Fig. 3) as well as the relation between their cell parameters ($a_{Cl} \approx 2{\cdot}c_{Br}$, $b_{Cl} \approx a_{Br}$, $c_{Cl} \approx 2{\cdot}b_{Br}$, $V_{Cl} \approx 4{\cdot}V_{Br}$). Both chloride and bromide analogs exhibit solid-to-solid state PTs above room temperature. Structural studies on both analogs' high temperature phases were undertaken, but due to considerable weakening of diffraction intensities they did not provide reliable results. Both analogs seem to crystallize in similar orthorhombic cells in the high temperature region. The models of the high temperature phases' structures were proposed. The best fit was obtained for the refinement in the $Pna2_1$ non-centrosymmetric space group with one $[CoX_4]^{2-}$ anion and two $(C_4H_{10}N)^+$ cations (Z' = 1) in the independent part of the structure for both chloride and bromide analogs. Thus, it may be stated that there is a common prototype high-symmetry phase for both analogs, which undergoes different deformations on cooling to room temperature.

$$\textbf{PCC}: \; a_{RT} \approx 2 \cdot b_{HT}, b_{RT} \approx c_{HT}, c_{RT} \approx 2 \cdot a_{HT}, V_{RT} \approx 4 \cdot V_{HT}$$

$$\textbf{PCB}: \; a_{RT} \approx c_{HT}, b_{RT} \approx a_{HT}, c_{RT} \approx b_{HT}, V_{RT} \approx V_{HT}$$

The crystal structure packing motif is common for both chloride and bromide analogs with the differences arising

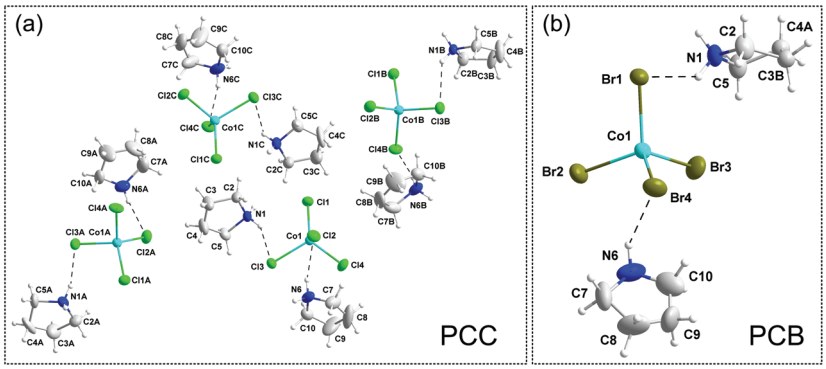

Fig. 2 The asymmetric unit of (a) **PCC** and (b) **PCB** at RT. Displacement ellipsoids are shown at the 20% probability level.

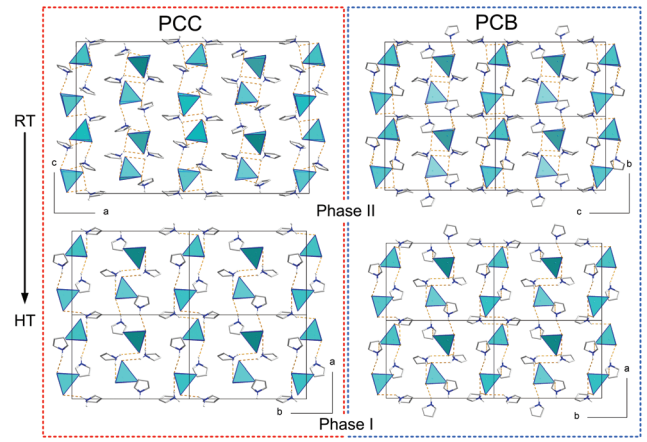

Fig. 3 Projection of the crystal structure packing of phases **II** (RT) and **I** (HT) of **PCC** and **PCB**.

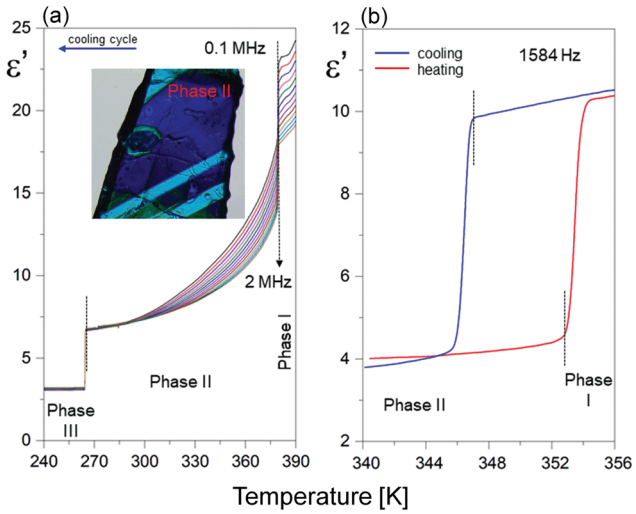

Fig. 4 Frequency dependencies of the real part of the dielectric constant (ε') at various temperatures for (a) **PCB** during cooling at 0.1 MHz; (b) **PCC** during heating and cooling at 1584 Hz.

from different deformations that take place during the HT → RT PTs. In general, both RT phases are built from tetrahedral $[CoX_4]^{2-}$ anions and $(C_4H_{10}N)^+$ cations in a 1 : 2 ratio. The cation atoms form 5-membered rings and are characterized by large thermal ellipsoids. The N atom positions were arbitrarily assigned to the atoms that possess the lowest thermal vibrations and produce the shortest donor–acceptor distances in the potential hydrogen bonds with halide anions. Each $(C_4H_{10}N)^+$ cation binds two neighbouring $[CoX_4]^{2-}$ anions through the formation of intermediate strength hydrogen bonds. Such type of bonding results in the formation of H-bonded layers, perpendicular to the *a*-axis direction in the chloride analog and columns, parallel to the *b*-axis direction, in the bromide analog.

The mechanism of PT in both chloride and bromide analogs, which occurs above-room temperature, involves mainly the reorientation of pyrrolidinium cations and the changes in their dynamic behaviour. The tetrahedra of $[CoX_4]^{2-}$ adjust themselves to the network of hydrogen bonds formed with amino-groups of cations and do not undergo considerable reorientations. In the RT phase of the chloride analog, four independent but geometrically very similar $[CoCl_4]^{2-}$ tetrahedra are present.

3.3 Dielectric measurements

The dielectric response (Fig. 4) confirmed the sequence of the PTs recorded in the calorimetric measurements for **PCA** and **PCB**. The temperature dependence of the real part of the complex electric permittivity in the frequency range 0.1–2 MHz for **PCB** (powdered sample) during the cooling cycle is shown in Fig. 4(a). It is clearly seen that **PCB** undergoes two PTs at 380 and 256 K which are accompanied by the rapid decrease in the ε' with $\Delta\varepsilon' \approx 4$–5 and $\Delta\varepsilon' \approx 3$, respectively. The PT (**II** → **III**) leads to a drastic breaking of the single crystal sample thus the measurements were carried out only during cooling. The insert in Fig. 4(a) shows the ferroelastic domain structure which was induced during the PT (**I** → **II**). A detailed description of the ferroelastic domains is presented in the ESI (section 4 (ESI) – Optical properties†). In the case of **PCC** the deformation of the sample through the lowest temperature PT (**II** → **III**) at 202 K is even more drastic than that for **PCB** thus the dielectric response ($\varepsilon'(T)$) is illustrated only around the ferroelastic transition (**I** → **II**) which is well reversible (Fig. 4(b)). One can observe a distinct dielectric increment, $\Delta\varepsilon' \approx 6$, measured at *ca.* 1.5 kHz. The low dielectric state (Phase **II**) represents 'switch off' and the high dielectric state (Phase **I**) indicates 'switch on' thus **PCC** is a good candidate for temperature-induced dielectric switchable materials.

3.4 ^{1}H NMR spin–lattice relaxation time studies

The temperature dependencies of the 25 MHz proton nuclear relaxation times (T_1) for **PCC** and **PCB** are shown in Fig. 5. Both temperature dependencies of T_1 are comparable and values of T_1 progressively grow from a fraction of a millisecond to more than three milliseconds. The T_1 values measured for **PCC** at high temperatures are about half as high as those for **PCB**, while the low-temperature data for both compounds are similar. It should be noted that such short times (typical ranges of T_1 are from milliseconds to seconds) are the result of the presence of ^{59}Co atoms possessing unpaired electrons.

^{1}H spin–lattice relaxation time in the studied compounds consists of two contributions: the first one, ^{1}H–^{1}H, results from the dipole–dipole interactions between protons of the pyrrolidinium cations and the second one, the ^{1}H–^{59}Co relaxation pathway, results from the dipole–dipole couplings of protons with the unpaired electron spin of ^{59}Co.[22,24,28,34,55–57]

$$\frac{1}{T_1} = \frac{1}{T_{1\,\mathrm{HH}}} + \frac{1}{T_{1\,\mathrm{HCo}}} = C_{\mathrm{HCo}}[3J(\omega_{\mathrm{H}}) + 7J(2\omega_{\mathrm{S}})] + C_{\mathrm{HH}}[J(\omega_{\mathrm{H}}) + 4J(2\omega_{\mathrm{H}})] \quad (1)$$

where the $J(\omega)$ are the spectral density functions being Fourier transforms of time correlation functions describing the sto-

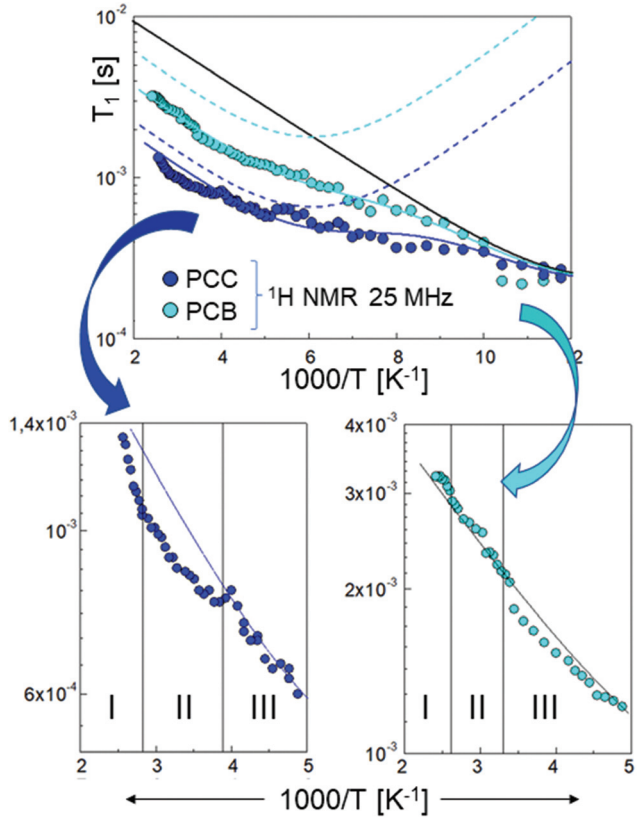

Fig. 5 ^{1}H spin–lattice relaxation time T_1 *versus* temperature for **PCB** (cyan points) and **PCC** (blue points) at 25 MHz and theoretical complete fit (solid lines) and components (dotted lines) obtained as a sum of two relaxation processes (eqn (4)).

chastic fluctuations of the dipole–dipole interaction. The spectral densities taken at ω_H and ω_S are associated with different correlation times, $\tau_{eff,1}$ and $\tau_{eff,2}$, respectively, defined as $\tau_{eff,1}^{-1} = \tau_c^{-1} + 1/T_{1,e}$ and $\tau_{eff,2}^{-1} = \tau_c^{-1} + 1/T_{2,e}$, where $T_{1,e}$ and $T_{2,e}$ are electron spin–lattice and electron spin–spin relaxation rates, respectively.[22,24,28,34,55–57] C_{HH} and C_{HCo} are relaxation dipole–dipole constants. The C_{HCo} relaxation constant is defined as:

$$C_{HCo} = \frac{2}{15} S(S+1) \left(\frac{\mu_0 \gamma_H \gamma_S \hbar}{4\pi r_{HCo}^3} \right)^2 \quad (2)$$

where r_{HCo} is an effective inter atomic distance, γ_H is the proton gyromagnetic ratio and γ_s is the electron gyromagnetic ratio, and S is the electron spin quantum number for Co(II) S = 3/2. As $\gamma_S/\gamma_H \cong 650$ the relaxation constants C_{HCo} and C_{HH} become comparable for $r_{HCo} \cong 8r_{HH}$. The T_{1HCo} contribution dominates, when r_{HCo} is smaller. As we noted above, the significantly shorter spin–lattice times T_1 for **PCC** and **PCB** measured here confirm that the observed relaxation is mostly due to the ^{1}H–^{59}Co dipole–dipole interactions and ^{1}H–^{1}H may be neglected. On the other hand, when we compare the contribution of both spectral density functions $J(\omega_S)$ and $J(\omega_H)$ to the overall relaxation we may conclude that the contribution associated with $J(\omega_S)$ can be neglected as well, since $\omega_S\tau_c \gg 1$. As a result, we obtain the simplified expression for the ^{1}H spin–lattice relaxation time

$$\frac{1}{T_1} = 3C_{HCo}J(\omega_H) = K_1 \frac{\tau_{c,1}}{1 + \omega_H{}^2\tau_{c,1}{}^2}. \quad (3)$$

This equation takes into account the fact that the correlation time τ_c is shorter than $T_{1,e}$ and usually $\tau_{eff,1} \cong \tau_{c,1}$. A cursory analysis of measured relaxation times T_1 *versus* temperature for **PCC** and **PCB** samples leads us to the conclusion that the observed dependencies require at least two relaxation mechanisms:

$$\frac{1}{T_1} = K_1 \frac{\tau_{c,1}}{1 + \omega_H{}^2\tau_{c,1}{}^2} + K_2 \frac{\tau_{c,2}}{1 + 4\omega_S{}^2\tau_{c,2}{}^2}. \quad (4)$$

In Fig. 5 are drawn the theoretical temperature dependencies of the relaxation time fitted using the above equation (see also Table S11†). As shown in Fig. 5 the theoretical line for **PCB** quite accurately coincides with the experimental data. In the case of **PCC**, the dynamic parameters are the same except the constant K_1, which is nearly three times smaller than that of **PCB**. This means that the low temperature relaxation process for both compounds is practically the same and the relaxation process due to the ^{1}H–^{59}Co dipole–dipole interactions at high temperatures is more sensitive to the physical properties of the sample. In the case of **PCC** the fit line matches the experimental points rather roughly, mainly due to the presence of several PTs. A conclusion from the T_1 measurements is that the lowest temperature transitions (**II** → **III**) are the most sensitive to PT in both compounds. The visible anomalies confirmed the main role of the pyrrolidinium cation dynamics in the PT mechanisms. The results of the M_2 measurements and discussion of possible motional state of cations with temperature for **PCC** and **PCB** are presented in the ESI (part 4†).

We can briefly compare the basic features of the compounds under investigation. Both materials exhibit two reversible PTs connected with the dynamics of pyrrolidinium cations. **PCC** and **PCB** are isomorphous in the paraelastic/ferroelastic phases, however in their intermediate phases (**II**) they differ somewhat from a structural point of view.

The crystal structure packing theme is common to both chloride and bromide analogs. Phase **II** is composed of tetrahedral anions $[CoX_4]^{2-}$ and cations $(C_4H_{10}N)^{+}$ in the ratio 1 : 2. The organic subnetwork consists of 5-membered pyrrolidine rings which are characterized by a significant dynamic disorder. A pseudo-one-dimensional structure is formed as a chain in which the $[CoX_4]^{2-}$ tetrahedra are bridged by pyrrolidinium cations *via* a hydrogen bond system. High-temperature PF (**II** → **I**) leads to an even greater disorder of the cations, while the positions of the $[CoX_4]^{2-}$ tetrahedra do not show significant changes in positions. There is a common high symmetry (orthorhombic) prototype phase for both analogs, which undergoes different deformations when cooled to room temperature, resulting in the differentiation of unit cell parameters. Significant entropy factors are consistent with the structural

picture that indicates significant changes in cation dynamics at the PT points for both compounds. Accordingly, all observed PTs are described by 'order–disorder' mechanisms. X-ray studies have shown that PT (**II** ↔ **I**) is accompanied by a change in the crystallographic system, and therefore these transformations belong to the class of ferroic transformations (2/*mFmm*2), according to the Aizu classification, accompanied by the induction of ferroelasticity. This image is consistent with the observation of crystals under a polarizing microscope for which the ferroelastic domain structures in phase **II** were observed for **PCC** and **PCB**. The proposed PT mechanisms were also confirmed by ^{1}H NMR studies. PT (**III** → **II**) turned out to be particularly active in both **PCC** and **PCB**, accompanied by clear anomalies in the T_1 *versus* $1/T$ characteristics. This proves that the change in the dynamic state of cations plays a key role in the mechanisms of low-temperature transitions. In turn, over phase **I** in **PCC** and **PCB** the pyrrolidine cations can perform twisted-envelope changes, and even rotations around the pseudo-five-fold axis of symmetry of the pyrrolidine ring.

3.5 Far-infrared magnetic spectroscopy

The EPR spectra of both compounds were of low quality revealing the presence of contamination with the spin Hamiltonian parameters substantially different from those of the main species seen in FIRMS (Fig. 6). In addition, the presence of four slightly different cobalt moieties in **PCC** apparently produces a set of spectra with slightly different parameters, making a precise simulation impossible. A large number of spectra were recorded with various microwave frequencies and the resonance fields were plotted as a function of frequency. In each case, zero-field resonances were found at frequencies consistent with those seen in FIRMS (Fig. 6). The FIRMS transitions, whose frequency does not change with the magnetic field (like those at 34, 37, 43 and 50 cm^{-1} in Fig. 6(b)), correspond to the phonon (vibrational) modes. Transitions observed at ~14 cm^{-1} in Fig. 6(a) and at 17 cm^{-1} in Fig. 6(b) are dependent on the magnetic field and therefore they are the magnetic transitions occurring between the ±1/2 and ±3/2 Kramers doublets. The frequency of these transitions at zero magnetic field is equal to the 'zero-field splitting' between the Kramers doublets and is related to the D and E parameters by $2\sqrt{D^2 + 3E^2}$.

The field-frequency dependencies reveal that both complexes exhibit large D, and E parameters of 7.8 and 2.1 cm^{-1}, respectively in **PCB** and 6.3, and 1.3 cm^{-1}, respectively in **PCC** (Fig. S14†). Although these D and E values produce correct zero-field frequencies, they must be treated as estimations due to low spectrum quality.

3.6 Magnetic studies – DC susceptibility

Magnetic data were acquired with the help of a SQUID magnetometer (MPMS, Quantum Design) at the applied field of B_0 = 0.5 T and, after correction for the underlying diamagnetism, transformed to the temperature dependence of the effective magnetic moment. Assuming g = 2.0, the expected high-temperature value for the S = 3/2 spin system is $\mu_{\text{eff}} = g[S(S+1)]^{1/2} = 3.87\mu_B$. The experimental data for **PCC** show a value of $\mu_{\text{eff}} = 4.53\mu_B$ at T = 300 K that implies $g > 2$ (Fig. 7). This value is almost constant on cooling down to 7 K and then it drops down owing to a zero-field splitting. The magnetization data at T = 2.0 and B_{DC} = 5.0 T saturate to $M_1 = M_{\text{mol}}/(N_A\mu_B) = 2.66$ which again confirms some zero-field splitting.

In fitting the magnetic data, the standard model of the zero-field splitting has been employed with the spin Hamiltonian (eqn (5)):

$$\hat{H}_k = D(\hat{S}_z^2 - \vec{S}^2/3)\hbar^{-2} + B\mu_B(g_z \cos\vartheta_k + g_{xy}\sin\vartheta_k)\hbar^{-1} \quad (5)$$

where k denotes grids distributed uniformly over the meridian (usually 16 grids) and ϑ_k is the polar angle. The eigenvalues enter the formulae of statistical thermodynamics for the magnetic susceptibility and magnetization; their mean values mimic the powder average.[58] An involvement of the rhombic zero-field splitting parameter E is probably a too ambitious task due to over parametrization.

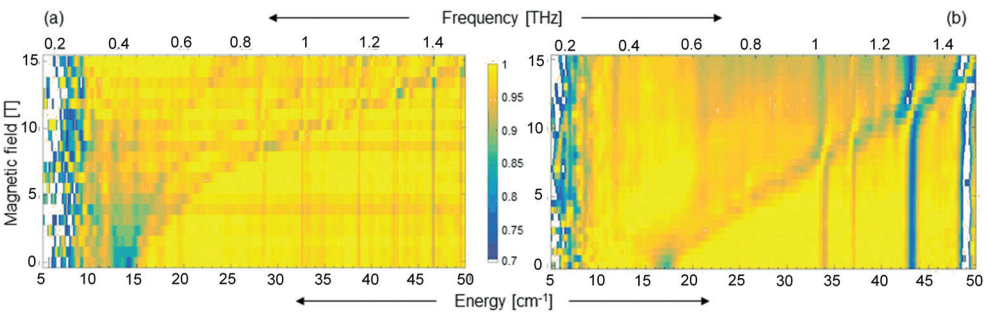

Fig. 6 (a) A color map of FIRMS resonances observed for **PCC** at 5 K showing a zero-field transition centered at 13–15 cm^{-1} evolving into powder patterns with an applied magnetic field. The tendency toward the blue color means the absorbance increases, whereas the yellow color corresponds to the transparent regions. The width of the zero-field transition is probably associated with the presence of 4 slightly different Co moieties (see Fig. 2); (b) a color map of FIRMS resonances observed for **PCB** at 5 K showing a zero-field transition at 17 cm^{-1} evolving into powder patterns with an applied magnetic field. Zero-field spectral features at 34, 37, 43 and 50 cm^{-1} correspond to the phonon (vibrational) modes, which are nominally field-independent until they anti-cross with the field-dependent transition at 17 cm^{-1}. The small shift of the phonon peaks with the applied magnetic field is a spectral manifestation of the spin–phonon coupling.

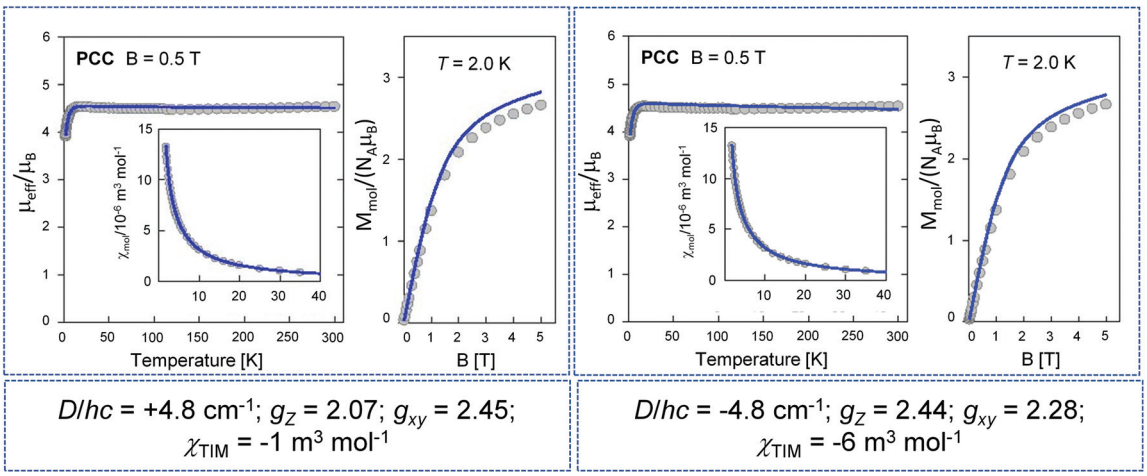

Fig. 7 Left – temperature evolution of the effective magnetic moment (inset: molar magnetic susceptibility in SI units) for **PCC**; right – field dependence of the magnetization per formula unit. Lines – fitted.

Both susceptibility and magnetization data with equal weights formed the error functional and its minimization gave the following set of magnetic parameters for **PCC**: D/hc = +4.8 cm^{-1}, g_z = 2.07, g_{xy} = 2.45; the additional correction refers to the temperature-independent magnetism χ_{TIM} = −1 m^3 mol^{-1} (it compensates uncertainties in the applied susceptibility corrections); the discrepancy factors for susceptibility and magnetization are $R(\chi)$ = 0.0063 and $R(M)$ = 0.069. The magnetic data can be fitted also with a reduced set $g_z = g_{xy}$ but then the reproduction of the magnetization is a bit worse. The sign reversal of D produces almost the same set of parameters, but values of g_{xy} and g_z are interchanged so that $D = \lambda(g_z - g_{xy})/2$ is fulfilled; the spin–orbit splitting parameter λ/hc = −172 cm^{-1} for Co(II).

The magnetic data for **PCB** are shown in Fig. 8. It can be seen that the fitting procedure gave D/hc = +7.0 cm^{-1}, g_z = 2.28, g_{xy} = 2.35, χ_{TIM} = 4.9 m^3 mol^{-1}, and the molecular-field correction zj/hc = −0.06 cm^{-1}; $R(\chi)$ = 0.0075 and $R(M)$ = 0.066.

In order to estimate the sign of the D-parameter in tetracoordinate Co(II) complexes a detailed inspection of the X-ray structure is helpful. Theoretical modelling using the generalized crystal field theory predicts that for the elongated tetrahedron (prolate disphenoid) of D_{2d} symmetry (two angles ≪ 109 deg) the D-parameter is negative. On the contrary, for a flattened tetrahedron (oblate disphenoid) of D_{2d} symmetry (two angles ≫ 109 deg) $D > 0$ holds true. **PCB** shows only a slight distortion from the tetrahedral geometry as Co–Br bond lengths are 2.395, 2.390, 2.386, and 2.393 Å. There are two bond angles Br–Co–Br ~ 111° which refer to a flattened tetrahedron for which $D > 0$ is predicted. The X-ray structure of **PCC** contains four different $[CoCl_4]^{2-}$ units and in all of them only two bond angles Cl–Co–Cl ~ 113°; this fact again leads to a prediction of a positive D.

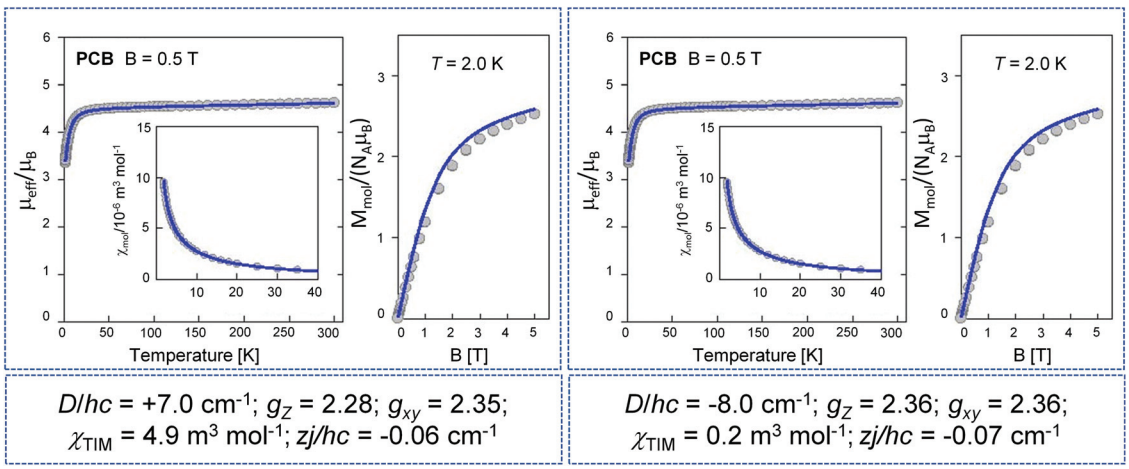

Fig. 8 Left – temperature evolution of the effective magnetic moment (inset: molar magnetic susceptibility in SI units) for **PCB**; right – field dependence of the magnetization per formula unit. Lines – fitted.

3.7 AC susceptibility

AC susceptibility data were acquired first at T = 2.0 K for a set of representative frequencies of the alternating field (f = 1.0, 11, 111, and 900 Hz) by ramping the magnetic field from zero to B_{DC} = 1.0 T; the working amplitude B_{AC} = 0.3 mT was used. Representative data for the complex **PCC** are displayed in Fig. 9. There is no absorption signal for both complexes (out-of-phase susceptibility component χ'') at the zero field owing to fast magnetic tunneling. With the increasing external field, this component for **PCC** rises, passes through a maximum, and then attenuates; such a behavior confirms that the complex **PCC** exhibits field supported slow magnetic relaxation. The position of the maximum, however, visibly depends upon the frequency f of the oscillating field.

Subsequent experiments for **PCC** have been performed with the amplitude B_{AC} = 0.3 mT and the fixed external magnetic field B_{DC} = 0.2 T (at which there is a maximum of the high-frequency signal) for a set of frequencies of the oscillating field ranging from f = 0.1–1500 Hz (Fig. 10). A dominating peak is seen at the out-of-phase susceptibility χ'' at frequencies f > 300 Hz. The peak position determines the relaxation time $\tau = 1/(2\pi f_{max})$ that is τ(HF) = 324 μs at T = 1.8 K. On heating this peak moves to higher frequencies so that the high-frequency relaxation time decreases as shown in Table S12;† numerical data were obtained through the fitting to the extended two-set Debye model. There is an on-set of the low-frequency (LF) relaxation channel seen as a minor peak in the χ'' *vs.* f graph. The extracted relaxation time enters the Arrhenius-like plot as shown in Fig. 11. The shift of the χ'' peak above the frequencies limited by the used hardware does not allow applying the high-temperature extrapolation to the traditional Orbach-process equation in order to obtain the barrier to spin reversal U_{eff} and the extrapolated relaxation time τ_0. To this end, the complex **PCC** at low temperature shows a field supported slow magnetic relaxation as a prerequisite of the single-ion magnetism.

Slow magnetic relaxation involving single or manifold relaxation processes has been found in numerous heptacoordinate, hexacoordinate, pentacoordinate, tetracoordinate and tricoordinate Co(II) complexes reported in recent years, although most of them exhibit magnetic relaxation only in an applied external magnetic field.[59–64] One of the ultimate requirements to observe this behavior is the presence of a large magnetic anisotropy, which generates an energy barrier for spin reversal, therefore many studies aimed at finding the principles of its controlled modification. On the basis of these studies it has been proved that the magnetic anisotropy of Co(II) complexes can be considerably influenced not only by the geometry of the

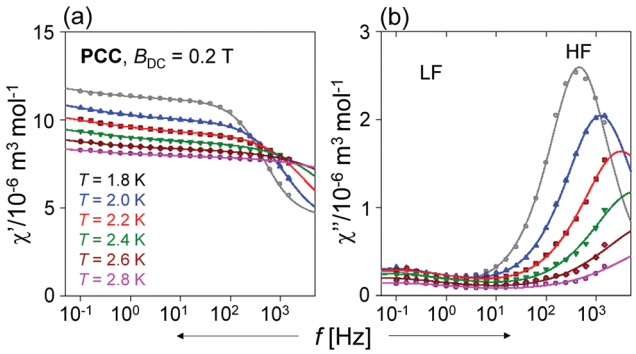

Fig. 10 Frequency dependence of the AC susceptibility components for **PCC** at B_{DC} = 0.2 T. Lines – fitted by the two-set Debye model.

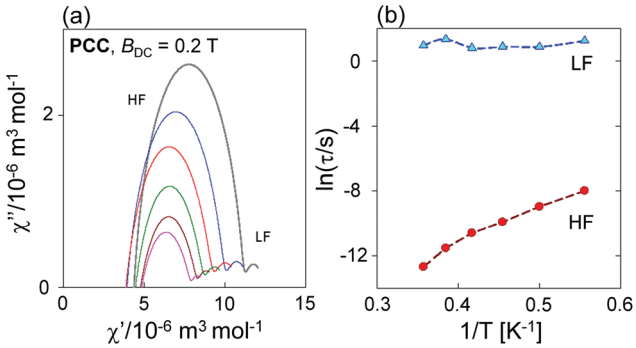

Fig. 11 Argand plot (left) and the Arrhenius-like plot (right) for **PCC**.

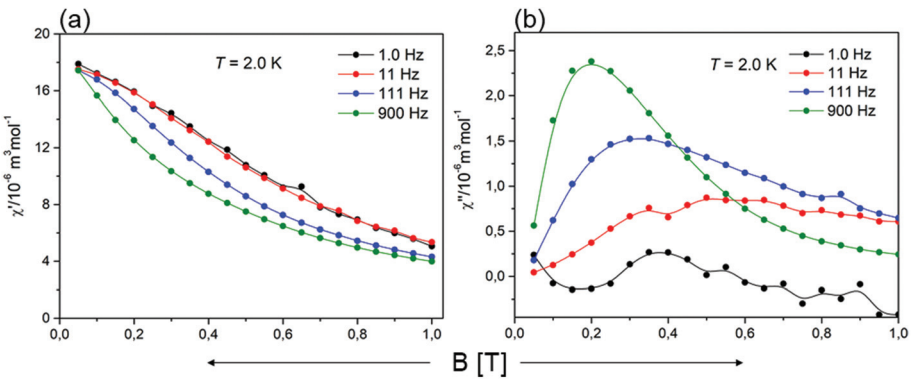

Fig. 9 Field dependence of the AC susceptibility components for **PCC** at T = 2.0 K for a set of frequencies of the AC field. Lines serve as guide to the eye.

coordination sphere but also by the type of terminal ligand and the nature of metal–ligand covalent bonding.[65–71] In particular for high-spin Co(II) tetracoordinate complexes with a tetrahedral geometry it has been shown that softer terminal ligands such as sulfur and oxygen are able to modify significantly the anisotropy of such a metal center.[50] Our study reveals that also other ligands such as halides hold the key to altering the magnitude and sign of the *D* value of complexes. The observation of a positive *D* value for both complexes is quite different from earlier prediction in the literature.[70] However Vaidya *et al.*[71] present examples of a series of mononuclear tetrahedral Co(II) complexes with a general molecular formula $[CoL_2X_2]$ [L = thiourea and X = Cl, Br, I] with the same sign but higher magnitude of the magnetic anisotropy for chloride and bromide analogs. This study reveals that heavier ligating atoms (such as iodide) with large spin–orbit coupling enhance the metal–ligand covalency, which tends to stabilize easy-axis magnetic anisotropy in contrast to smaller metal–ligand covalency of the Co–Cl and Co–Br bonds stabilizing easy-plane magnetic anisotropy in tetrahedral Co(II) complexes. A higher value of *D* in **PCB** than **PCC** confirms this hypothesis. The smaller magnitude of *D* in our complexes can be the result of only a slight distortion from the tetrahedral geometry realized by the four similar Co–X bonds. Also, we rationalize that the absence of slow magnetic relaxation behavior in **PCC** and **PCB** under zero external magnetic field is due to the lack of a pure ground state in both complexes, and further the large *E*/*D* value effectively triggers QTM rather than a thermally assisted Orbach process.

4. Conclusions

Single crystals of two organic–inorganic hybrids based on pyrrolidinium-tetrahalidocobaltates were successfully synthesized. They have 0D structures with isolated $[CoX_4]^{2-}$ tetrahedra separated by disordered pyrrolidinium cations. A stepwise ordering of organic cations leads to two PTs: **PCC** at 347/353 K (**I** ↔ **II**) and 202/257 K (**II** ↔ **III**) and **PCB** at 380/381 K (**I** ↔ **II**) and 256/302 K (**II** ↔ **III**). Optical observations under polarized light and single crystal X-ray diffraction measurements revealed that for both compounds the ferroic PT (**I** → **II**) belongs to the ferroelastic type *mm*2*F*2/*m* in the Aizu notation. This work confirms the assumption that introducing mobile organic cations into the tetrahalidocobaltate network might construct compounds with multiple properties. The DC magnetic data show magnetic anisotropy, which was confirmed by the high-field HF EPR measurement together with the FIRMS method for determining the exact large *D* value for **PCC** (4.80 cm^{-1}) and **PCB** (7.00 cm^{-1}). The AC susceptibility data confirm that only complex **PCC** exhibits a slow magnetic relaxation under a small applied DC field with two relaxation modes. To generalize, surrounding a tetrahedral Co(II) ion by heavier donor ligands of similar *p*/*s* strength ought to stabilize easy-plane anisotropy with a rather large *E*/*D* ratio.

Author contributions

The manuscript was written through contributions of all authors. All authors have given approval to the final version of the manuscript.

Conflicts of interest

There are no conflicts to declare.

Acknowledgements

The magnetic measurements were supported by the University of Wroclaw program IDUB (BPIDUB. 4610.17.2021.KP.B) (A. B.). The National High Magnetic Field Laboratory is supported by National Science Foundation Cooperative Agreement No. DMR-1644779 (A. O., M. O). Slovak Grant Agencies (APVV 16-0039, APVV 18-0016, VEGA 1/0919/17 and VEGA 1/0013/18) are acknowledged for the financial support.

References

1 S. Sawada, Y. Shiroishi and A. Yamamoto, *Ferroelectrics*, 1978, **21**, 413–414.
2 H. Shimizu, N. Kokubo, N. Yasuda and S. Fujimoto, *J. Phys. Soc. Jpn.*, 1980, **49**, 223–229.
3 E. Styczeń, A. Pattek-Janczyk, M. Gazda, W. K. Jóźwiak, D. Wyrzykowski and Z. Warnke, *Thermochim. Acta*, 2008, **480**, 30–34.
4 E. Styczeń, W. K. Jóźwiak, M. Gazda, D. Wyrzykowski and Z. Warnke, *J. Therm. Anal. Calorim.*, 2008, **91**, 979–984.
5 J. Zubillaga, A. Lopez-Eharri and M. J. Tello, *J. Phys. C: Solid State Phys.*, 1988, **21**, 4417–4423.
6 R. Clay, J. Murray-Rust and P. Murray-Rust, *Acta Crystallogr., Sect. B: Struct. Crystallogr. Cryst. Chem.*, 1975, **31**, 289–292.
7 M. R. Pressprich, M. R. Bond and R. D. Willett, *Phys. Rev. B: Condens. Matter Mater. Phys.*, 1991, **43**, 13549–13558.
8 A. Lopez-Echarri, M. J. Tello, C. Socias and J. Herreros, *J. Phys. C: Solid State Phys.*, 1985, **18**, 2631–2642.
9 J. A. Barreda-Argüeso, L. Nataf, Y. Rodríguez-Lazcano, F. Aguado, J. González, R. Valiente, F. Rodríguez, H. Wilhelm and A. P. Jephcoat, *Inorg. Chem.*, 2014, **53**, 10708–10715.
10 Y. Sui, Y. S. Zhong, W. T. Chen, G. X. Zhang, C. L. Liu and D. S. Liu, *J. Phys. Chem. C*, 2019, **123**, 14647–14651.
11 Q. Ji, L. Li, S. Deng, X. Cao and L. Chen, *Dalton Trans.*, 2018, **47**, 5630–5638.
12 L. Z. Chen, D. D. Huang, Q. J. Pan and J. Z. Ge, *RSC Adv.*, 2015, **5**, 13488–13494.
13 X. N. Hua, C. R. Huang, J. X. Gao, Y. Lu, X. G. Chen and W. Q. Liao, *Dalton Trans.*, 2018, **47**, 6218–6224.
14 F. Issaoui, W. Amamou, M. Bekri, F. Zouari, F. Dhahri and M. A. Valente, *J. Mol. Struct.*, 2019, **1189**, 175–180.

15 D. H. Wu and L. Jin, *Inorg. Chem. Commun.*, 2012, **23**, 98–102.
16 M. F. Mostafa, A. A. Youssef, T. S. El Dean, A. M. Mostafa and I. S. A. Farag, *Cryst. Res. Technol.*, 2008, **43**, 547–560.
17 V. Kapustianyk, S. Semak, M. Panasyuk, M. Rudko and V. Rudyk, *Phase Transitions*, 2019, **92**, 396–405.
18 M. F. Mostafa, S. S. El-khiyami and S. K. Alal, *J. Phys. Chem. Solids*, 2018, **118**, 6–13.
19 A. Sen, S. Roy, S. C. Peter, A. Paul, U. V. Waghmare and A. Sundaresan, *J. Solid State Chem.*, 2018, **258**, 431–440.
20 K. Horiuchi, *Phys. Stat. Sol. A*, 2004, **201**, 723–726.
21 V. E. Vasiliev, M. Rudiak, A. Bobrova and V. M. Varikash, *Tverd. Tela*, 1987, **29**, 1539.
22 M. M. Abdelkader and M. Abdelmohsen, *Mater. Res. Express*, 2019, **6**, 025608.
23 C. Ji, S. Liu, S. Han, K. Tao, Z. Sun and J. Luo, *Angew. Chem., Int. Ed.*, 2018, **57**, 16764–16767.
24 A. Piecha-Bisiorek, A. Bieńko, R. Jakubas, R. Boča, M. Weselski, V. Kinzhybalo, A. Pietraszko, M. Wojciechowska, W. Medycki and D. Kruk, *J. Phys. Chem. A*, 2016, **120**, 2014–2021.
25 M. Wojciechowska, A. Gągor, A. Piecha-Bisiorek, R. Jakubas, A. Cizman, J. K. Zaręba, M. Nyk, P. Zieliński, W. Medycki and A. Bil, *Chem. Mater.*, 2018, **30**, 4597–4608.
26 D. M. S. Martins, D. S. Middlemiss, C. R. Pulham, C. C. Wilson, M. T. Weller, P. F. Henry, N. Shankland, K. Shankland, W. G. Marshall, R. M. Ibberson, K. Knight, S. Moggach, M. Brunelli and C. A. Morrison, *J. Am. Chem. Soc.*, 2009, **131**, 3884–3893.
27 H. Ishida, Y. Furukawa, S. Sato and S. Kashino, *J. Mol. Struct.*, 2000, **524**, 95–103.
28 B. Bednarska-Bolek, R. Jakubas, G. Bator and J. Baran, *J. Mol. Struct.*, 2002, **614**, 151–157.
29 R. Jakubas, B. Bednarska-Bolek, J. Zaleski, W. Medycki, K. Hołderna-Natkaniec, P. Zieliński and M. Gałązka, *Solid State Sci.*, 2005, **7**, 381–390.
30 D. Nilsen, R. Larsen, K. Emerson, G. V. Rubenacker, Z. Ping and J. E. Drumheller, *Inorg. Chem.*, 1990, **29**, 2887–2888.
31 M. Wei, R. D. Willett, D. Teske, K. Subbaraman and J. E. Drumheller, *Inorg. Chem.*, 1996, **35**, 5781.
32 Y. Zhang, W. Liao, D. Fu, H. Ye, M. Liu, Z. Chen and R. Xiong, *Adv. Mater.*, 2015, **27**, 3942–3946.
33 Y. Zhang, W. Q. Liao, D. W. Fu, H. Y. Ye, Z. N. Chen and R. G. Xiong, *J. Am. Chem. Soc.*, 2015, **137**, 4928–4931.
34 M. Ksiądzyna, A. Gągor, A. Piecha-Bisiorek, A. Ciżman, W. Medycki and R. Jakubas, *J. Mater. Chem. C*, 2019, **7**, 10360–10370.
35 Y. Rechkemmer, F. D. Breitgoff, M. Van Der Meer, M. Atanasov, M. Hakl, M. Orlita, P. Neugebauer, F. Neese, B. Sarkar and J. Van Slageren, *Nat. Commun.*, 2016, **7**, 10467–10474.
36 K. Chakarawet, P. C. Bunting and J. R. Long, *J. Am. Chem. Soc.*, 2018, **140**, 2058–2206.
37 A. Eichhöfer, Y. Lan, V. Mereacre, T. Bodenstein and F. Weigend, *Inorg. Chem.*, 2014, **53**, 1962–1974.
38 J. M. Zadrozny and J. R. Long, *J. Am. Chem. Soc.*, 2011, **133**, 20732–20734.
39 J. M. Zadrozny, J. Liu, N. A. Piro, C. J. Chang, S. Hill and J. R. Long, *Chem. Commun.*, 2012, **48**, 3927–3929.
40 T. Jurca, A. Farghal, P. H. Lin, I. Korobkov, M. Murugesu and D. S. Richeson, *J. Am. Chem. Soc.*, 2011, **133**, 15814–15817.
41 F. Habib, O. R. Luca, V. Vieru, M. Shiddiq, I. Korobkov, S. I. Gorelsky, M. K. Takase, L. F. Chibotaru, S. Hill, R. H. Crabtree and M. Murugesu, *Angew. Chem., Int. Ed.*, 2013, **52**, 11290–11293.
42 D. M. Piñero Cruz, D. N. Woodruff, I. R. Jeon, I. Bhowmick, M. Secu, E. A. Hillard, P. Dechambenoit and R. Clérac, *New J. Chem.*, 2014, **38**, 3443–3448.
43 J. Vallejo, I. Castro, R. Ruiz-García, J. Cano, M. Julve, F. Lloret, G. De Munno, W. Wernsdorfer and E. Pardo, *J. Am. Chem. Soc.*, 2012, **134**, 15704–15707.
44 X. C. Huang, C. Zhou, D. Shao and X. Y. Wang, *Inorg. Chem.*, 2014, **53**, 12671–12673.
45 L. Chen, J. Wang, J. M. Wei, W. Wernsdorfer, X. T. Chen, Y. Q. Zhang, Y. Song and Z. L. Xue, *J. Am. Chem. Soc.*, 2014, **136**, 12213–12216.
46 A. E. Ion, S. Nica, A. M. Madalan, S. Shova, J. Vallejo, M. Julve, F. Lloret and M. Andruh, *Inorg. Chem.*, 2015, **54**, 16–18.
47 S. Vaidya, S. Tewary, S. K. Singh, S. K. Langley, K. Murray, Y. Lan, W. Wernsdorfer, G. Rajaraman and M. Shanmugam, *Inorg. Chem.*, 2016, **55**, 9564–9578.
48 E. A. Suturina, J. Nehrkorn, J. M. Zadrozny, J. Liu, M. Atanasov, T. Weyhermueller, D. Maganas, S. Hill, A. Schnegg, E. Bill, J. R. Long and F. Neese, *Inorg. Chem.*, 2017, **56**, 3102–3118.
49 A. K. Mondal, M. Sundararajan and S. A. Konar, *Dalton Trans.*, 2018, **47**, 3745–3754.
50 J. M. Zadrozny, J. Telser and J. R. Long, *Polyhedron*, 2013, **64**, 209–217.
51 M. R. Saber and K. R. Dunbar, *Chem. Commun.*, 2014, **50**, 12266–12269.
52 Agilent, *CrysAlis PRO*, Agilent Technologies Ltd, Yarnton, Oxfordshire, England, 2014.
53 G. M. Sheldrick, *Acta Crystallogr., Sect. C: Struct. Chem.*, 2015, **71**, 3–8.
54 O. V. Dolomanov, L. J. Bourhis, R. J. Gildea, J. A. K. Howard and H. Puschmann, *J. Appl. Crystallogr.*, 2009, **42**, 339–341.
55 J. D. Epperson, Li.-J. Ming, B. D. Woosley, G. R. Baker and G. R. Newkome, *Inorg. Chem.*, 1999, **38**, 4498–4502.
56 B. Bednarska-Bolek, R. Jakubas, W. Medycki, D. Nowak and J. Zaleski, *J. Phys.: Condens. Matter*, 2002, **14**, 3129–3142.
57 W. Medycki, J. Świergiel, K. Hołderna-Natkaniec, K. Jurga and R. Jakubas, *Solid State Nucl. Magn. Reson.*, 2004, **25**, 129–132.
58 R. Boča, *A Handbook of Magnetochemical Formulae*, Elsevier, Amsterdam, 2012.
59 C. Rajnák, A. Packová, J. Titiš, J. Miklovič, J. Moncol and R. Boča, *Polyhedron*, 2016, **110**, 85–92.
60 L. Smolko, J. Černák, M. Dušek, J. Miklovič, J. Titiš and R. Boča, *Dalton Trans.*, 2015, **44**, 17565–17571.

61 A. Świtlicka, B. Machura, M. Penkala, A. Bieńko, D. C. Bieńko, J. Titiš, C. Rajnák, R. Boča and A. Ozarowski, *Inorg. Chem. Front.*, 2020, **7**, 2637–2650.
62 R. Boča, J. Miklovič and J. Titiš, *Inorg. Chem.*, 2014, **53**, 2367–2369.
63 C. Rajnák, J. Titiš, O. Fuhr, M. Ruben and R. Boča, *Inorg. Chem.*, 2014, **53**, 8200–8202.
64 A. Świtlicka, B. Machura, M. Penkala, A. Bieńko, D. C. Bieńko, J. Titiš, C. Rajnák, R. Boča, A. Ozarowski and M. Ozerov, *Inorg. Chem.*, 2018, **57**, 12740–12755.
65 K. Fukui, H. Ohya-Nishinuchi and N. Hirota, *Bull. Chem. Soc. Jpn.*, 1991, **64**, 1205–1212.
66 K. Fukui, N. Kojima, H. Ohya-Nishinuchi and N. Hirota, *Inorg. Chem.*, 1992, **31**, 1338–1344.
67 D. Maganas, S. Milikisyants, J. M. A. Rijnbeek, S. Sottini, N. Levesanos, P. Kyritsis and E. J. J. Groenen, *Inorg. Chem.*, 2010, **49**, 595–605.
68 D. Maganas, S. Sottini, P. Kyritsis, E. J. J. Groenen and F. Neese, *Inorg. Chem.*, 2011, **50**, 8741–8754.
69 S. Vaidya, A. Upadhyay, S. K. Singh, T. Gupta, S. Tewary, S. K. Langley, J. P. S. Walsh, K. S. Murray, G. Rajaraman and M. Shanmugam, *Chem. Commun.*, 2015, **51**, 3739–3742.
70 S. Vaidya, S. Tewary, S. K. Singh, S. K. Langley, K. Murray, Y. Lan, W. Wernsdorfer, G. Rajaraman and M. Shanmugam, *Inorg. Chem.*, 2016, **55**, 9564–9578.
71 S. Vaidya, S. K. Singh, P. Shukla, K. Ansari, G. Rajaraman and M. Shanmugam, *Chem. – Eur. J.*, 2017, **23**, 9546–9559.

